IOP Publishing   Bioinspir. Biomim. 17 (2022) 046004   https://doi.org/10.1088/1748-3190/ac6375

Bioinspiration & Biomimetics

RECEIVED
4 October 2021

REVISED
30 March 2022

ACCEPTED FOR PUBLICATION
1 April 2022

PUBLISHED
13 May 2022

PAPER

Force scaling and efficiency of elongated median fin propulsion

Mohammad I Uddin, Gonzalo A Garcia and Oscar M Curet*

Department of Ocean and Mechanical Engineering, Florida Atlantic University, Boca Raton, FL, United States of America
* Author to whom any correspondence should be addressed.

E-mail: ocuret@fau.edu

Keywords: fish swimming, bio-propulsion, unmanned underwater vehicle, fin, efficiency

Abstract

Several fishes swim by undulating a thin and elongated median fin while the body is mostly kept straight, allowing them to perform forward and directional maneuvers. We used a robotic vessel with similar fin propulsion to determine the thrust scaling and efficiency. Using precise force and swimming kinematics measurements with the robotic vessel, the thrust generated by the undulating fin was found to scale with the square of the relative velocity between the free streaming flow and the wave speed. A hydrodynamic efficiency is presented based on propulsive force measurements and modelling of the power required to oscillate the fin laterally. It was found that the propulsive efficiency has a broadly high performance versus swimming speed, with a maximum efficiency of 75%. An expression to calculate the swimming speed over wave speed was found to depend on two parameters: A_p/A_e (ratio between body frontal area to fin swept area) and C_D/C_x (ratio of body drag to fin thrust coefficient). The models used to calculate propulsive force and free-swimming speed were compared with experimental results. The broader impacts of these results are discussed in relation to morphology and the function of undulating fin swimmers. In particular, we suggest that the ratio of fin and body height found in natural swimmers could be due to a trade-off between swimming efficiency and swimming speed.

1. Introduction

Certain fishes generate thrust by sending traveling waves along a thin and elongated membrane while the body is kept mainly straight. Typically, when fishes swim using this propulsion method, the wavelength of the travelling wave is equal to or shorter than the fin length, resulting in one or more wavelengths present along the fin. This type of propulsion with undulations along an elongated median fin (we will refer to it as ribbon-fin propulsion) has been of particular interest due to its capabilities to generate and control thrust. This allows for impressive maneuvers including swimming forward, backward, and vertically, hovering, as well as rapid changes of direction [1, 2]. Although there have been previous studies on the thrust generation of ribbon fin-like propulsion, there has not been an experimental study to investigate the thrust generation and efficiency as the flow around the fin changes. In this work, we used a robotic undulating fin to experimentally study how the longitudinal propulsive force and the efficiency change as flow speed is varied. Using experimental data, we present an empirical scaling law and evaluate the propulsive efficiency and the trade-off between swimming speed and efficiency.

Ribbon fin propulsion is found in different body configurations (figure 1) including that of a single fin along the ventral body side (gymnotiform), a dorsal side (amiiform), or with two fins along the dorsal and ventral sides (ballistiform). Although different forms of elongated median fin are observed across fish species, their primary function is to generate propulsive force. However, some fish, for example bowfin (*Amia calva*), can switch between undulating fin propulsion to body-caudal propulsion depending on the swimming speed [4]. Borazjani and Sotiropoulos [5] conducted numerical simulation with different combinations of carangiform and anguilliform swimmers. Their work showed that the wake structure depends on Strouhal number. Moreover, recent numerical studies on carangiform [6, 7] and anguilliform [7, 8] swimmers showed that different wavelengths suit different forms of fishes. Youngerman *et al* [9] studied the fin kinematics of free-swimming ghost knifefish and this study indicates an active control in the curvature of the fin rays.

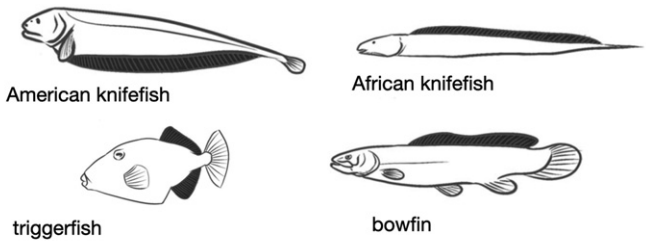

Figure 1. Undulating fin configuration in different fish species: ventral (American knifefish), dorsal (African knifefish), ventral and dorsal (triggerfish). Some fish modulate from caudal to undulating fin propulson depending on swimming speed (bowfin). [4] John Wiley & Sons. © 2013 Wiley Periodicals, Inc.

Robotic systems have also been critical in understanding the mechanics of fish swimming [10–14]. For example, Quinn *et al* [15] investigated the scaling of the propulsive performance of a heaving flexible panel. Yu and Huang [16] constructed a hydrodynamic thrust scaling formation for an undulatory propulsor. Hu and Yu [17] numerically investigated undulatory braking motion hydrodynamics. Recent studies [18–21] have demonstrated that the mean thrust generated by oscillating foils is independent of swimming speed. Thus, an oscillating foil generates the same amount of mean thrust regardless of the incoming flow speed. One pressing question is to determine how general this finding is for other biological propulsion (e.g. undulating fin, anguilliform propulsion etc) or if it is a specific feature of oscillating foils.

Fundamental theoretical work by Lighthill [22], Lighthill and Blake [23] and Wu [24], models the thrust generated by a 2D waving plate along the longitudinal axis to be proportional to the wave speed and incoming flow as follows

$$T \propto V^2 - U^2 \tag{1}$$

where $V = f\lambda$ is the wave velocity (λ = wavelength and f = fin oscillating frequency) and U is the swimming speed. In this case, the fin is assumed to be of infinite height and interacting with a 2D flow. Neveln *et al* [25] showed that undulating fin propulsion produces 3D flow structure. More recent work based on a finite undulating fin, where the fin pivots along the top part of the fin length, have suggested that the propulsive force scales as

$$T \propto (V - U)\,|(V - U)| \tag{2}$$

where $(V - U)$ can be represented as the relative velocity, V_{rel}, between the wave speed V and the swimming speed U. This expression for thrust generation has been based on both computational [26, 27] and experimental work ([25, 27–29]). However, these works are based on force measurements with no incoming flow conditions and limited free-swimming experiments. In this work, we used a robotic system to (1) experimentally determine the propulsive force behavior as flow speed and fin kinematics are varied; (2) present a metric of the hydrodynamic efficiency and (3) corroborate the force measurements (tether condition) and associated scaling relationship against free-swimming conditions.

Previous work has conducted quantitative analysis on fin kinematics and thrust generated from undulating fin propulsion using computational simulation [30], live animals [3, 4] and robotic devices [28, 29]. The robotic prototypes have been tested whilst stationary and freely moving to characterize propulsive force for different actuation parameters [28, 31, 32]. Particle image velocimetry experiments led to a better understanding of the flow structure in the vicinity of the undulating fin propulsion [32]. A recent study [34] experimentally investigated the potential momentum enhancement of an undulating fin interacting with different body heights. In addition, the undulating fin has been explored for power generation [33].

The hydrodynamic efficiency, commonly known as Froude propulsive efficiency [22], is given by

$$\eta = \frac{TU}{P} \tag{3}$$

where P is the mean total power. Previous work estimated mean total power as a sum of wake power and thrust power that generates forward thrust [22, 24, 35]. For an infinite wavy plate without any body attached to it [22, 24], the propulsive efficiency has been modeled as

$$\eta = 1 - \frac{V - U}{2V}. \tag{4}$$

A similar expression has been used for undulatory propulsion (e.g. anguilliform and carangiform swimming) [22, 35]. However, for undulating ribbon fin propulsion where the generated thrust by the undulating fin and the main drag (body) are mostly separate, this expression has significant limitations. First, when the incoming flow velocity is equal to that of the traveling wave ($U = V$), the hydrodynamic efficiency is equal to one. However, in this situation the generation of thrust should be equal to zero, thus the hydrodynamic efficiency should be also equal to zero.

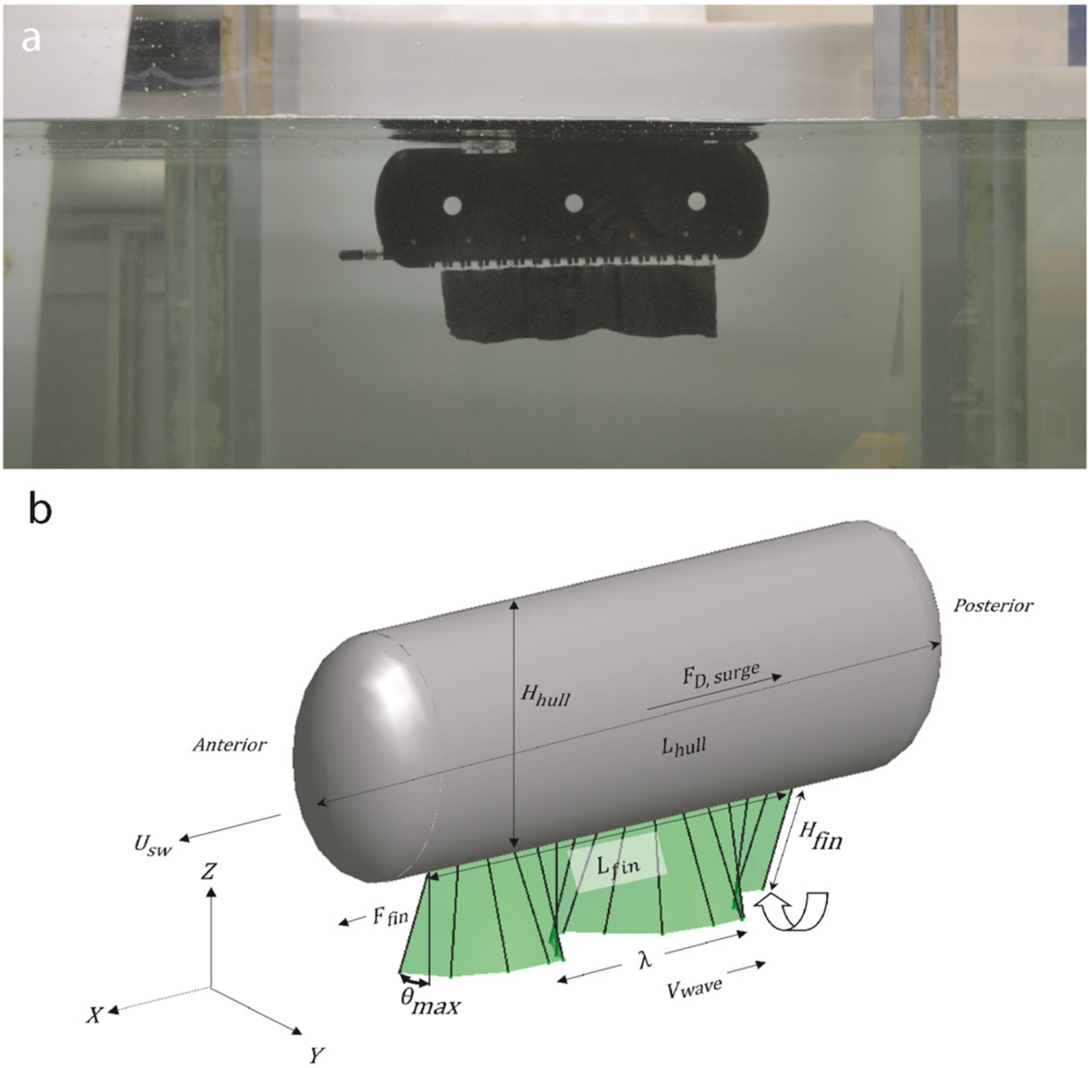

Figure 2. Robotic vessel with undulating fin propulsion. (a) Snapshot of the robotic vessel during a free-swimming test in a tank. The vessel propels itself using a flexible undulating fin controlled by 16 independent rays. Three white markers were used to track the motion of the vessel. (b) Schematic of the vessel showing key parameters of the system.

In the other extreme, when the incoming flow velocity tends to zero the hydrodynamic efficiency tends to 0.5. However, if there is no swimming speed ($U = 0$), the efficiency should also tend zero.

In this work, a robotic vessel with undulating fin propulsion (figure 2) was used to conduct all the experiments. We measured the net force and swimming speed generated at different fin kinematics. The robotic system in this work was used in different flow conditions, with prescribed motion and flow where the system was attached to a load cell and for free-swimming (self-propelled) conditions. All force measurements were conducted with the robot mounted on a load cell with imposed flow around the fin and vessel. Those experiments were used to determine the scaling of the thrust generation as the flow around the fin and fin kinematics were varied. Then, using drag measurements from the body and the thrust model, we were able to predict the quasi-steady state free swimming speed and compare it with free-swimming experiments. We present a mathematical formulation for hydrodynamic efficiency for undulating fin propulsion. Finally, we discuss the broader impact of the present work to understand engineered and biological swimmers with undulating fin propulsion.

2. Theoretical considerations

Here we present the forces and the equations of motion associated with an undulating rectangular fin attached to a rigid body. All forces acting on the robotic fish are considered decoupled from each other. Thus, all force components will be estimated separately and then the resultant at any direction will be computed by the super-position principle.

2.1. Undulating fin force

The undulating ribbon fin in fishes undergoes complex motion, which can be approximated as a combination of sinusoids. In the present work, we will consider only one sinusoidal motion in the fin.

2.2. Model 1: thrust force proportional to $\left(V^2 - U^2\right)$

As discussed, Lighthill and others [22, 24] have modeled the propulsive-longitudinal force along the fin as

$$T_1 = C_k\left(V^2 - U^2\right). \tag{5}$$

Here, C_k is the force coefficient, which is a function of added mass, fin actuation parameters and fluid properties [36]. $V = f\lambda$ is the wave speed. Throughout the present work, we will refer to this force modeling as model 1. V is considered to be travelling in the anterior to posterior direction. U is the flow velocity along negative x-axis (from anterior to posterior) relative to the vessel (or fish). U, as defined before, is the incoming flow relative to the body. When the vessel is freely swimming, we use the notation U_{sw}.

2.3. Model 2: thrust force proportional to $(V - U)^2$

More recent experimental work on undulating fin propulsion suggests that the force generated in the surge direction is a quadratic function of the relative velocity, that is, as stated earlier, the difference between wave velocity and flow velocity, $V_{\mathrm{rel}} = V - U$ [28, 31]. According to these findings, the propulsive force is a second order function of V_{rel} and can be expressed as

$$T_2 = \frac{1}{2}C_x\rho A_{\mathrm{e}}V_{\mathrm{rel}}\left|V_{\mathrm{rel}}\right| \tag{6}$$

C_x is the nondimensional force coefficient along the longitudinal axis of the fin and ρ is the density of fresh water (1000 kg m^{-3}). A_{e} is the characteristic area for fin force, which is the projected area swept by the fin tip. This area for a fin with sinusoidal motion is given by

$$A_{\mathrm{e}} = 2L_{\mathrm{fin}}H_{\mathrm{fin}}\,\sin\left(\theta_{\mathrm{max}}\right) \tag{7}$$

where H_{fin} is the fin height, L_{fin} the fin length, and θ_{max} the maximum angular deflection (figure 2(b)).

2.4. Hull drag force

The hull of the robotic vessel incurs a drag force when fluid flows relative to the body. For a blunt body the drag of the hull can be estimated as

$$D_{\mathrm{hull}} = \frac{1}{2}C_{\mathrm{D}}\rho A_{\mathrm{p}}U^2 \tag{8}$$

where C_{D} is the nondimensional drag coefficient for the body, and A_{p} is the frontal projected area. For the robotic vessel with an ellipsoidal cross section, $A_{\mathrm{p}} = \frac{\pi}{4}H_{\mathrm{hull}}W_{\mathrm{hull}}$, where H_{hull} and W_{hull} are the height and width of the hull, respectively.

2.5. Equation of surge motion

The equation of motion along the longitudinal direction (surge direction) for a rigid body with ribbon fin propulsion is given by its inertia, added mass, drag force (due to the body) and thrust force (generated by fin). For the single degree of freedom system in surge motion, the force balance is as follows

$$M\left(1 + A_x\right)\ddot{x} = F_{\mathrm{net}} - D_{\mathrm{hull}} \tag{9}$$

where M = mass of the vessel, A_x = added mass coefficient on the positive x-axis, $\ddot{x} = \frac{\mathrm{d}^2x}{\mathrm{d}t^2}$, acceleration of the vessel along the positive x-axis, D_{hull} = drag force of the body, against the motion, on the negative x-axis and F_{net} = net fin force, along the positive x-axis. This force can be expressed as $F_{\mathrm{net}} = T - D_{\mathrm{fin}}$, where T is the thrust generated by the fin, and D_{fin} is the drag force incurred by the undulating ribbon fin.

For the steady free-swimming condition, inertia force becomes zero, which leaves the net fin force equal to the drag force of the vessel. It should be noted that, along with mean longitudinal force, undulating fin propulsion is accompanied by heave force along the vertical axis. Sometimes, fishes trim their body to take advantage of this force, presumably for depth control and surge force increase. However, the present work considered all experiments to be done with zero trim in the vessel, and surge force is generated solely by fin force along the longitudinal direction.

2.6. Power and efficiency

We consider that the total hydrodynamic power input to the robotic fin to actuate the robotic fin will be the sum of thrust power in the forward surge direction (TU) and lateral power (P_{lat}) required to actuate the fin in sinusoidal motion. This lateral power will be estimated based on a nonviscous dynamic pressure model and added mass due to the oscillation of the fin. Note that this power takes into consideration the hydrodynamic power without the power to stretch the membrane or the inertia of the actual fin.

Measurement of the lateral hydrodynamic power, P_{lat}, is not trivial. Thus, we estimate this power based on the nonviscous dynamic pressure model and the added mass of the fin. For this, we consider the fin consisting of N elements with equal dimensions of Δx and Δz along the x- and z-axis, respectively, (assuming zero thickness of the fin). For the ith element, the power required at time t to move the element through fluid will be the sum of the power due to inertia force and the drag force acting on the element

$$P_{\mathrm{lat},i}\left(t\right) = F_{\mathrm{lat},i}(t)v_i(t) = \left(F_{\mathrm{v},i}\left(t\right) + F_{\mathrm{a},i}(t)\right)v_i(t). \tag{10}$$

Here, $F_{\mathrm{lat},i}(t)$ is the instantaneous force needed to actuate the element area, and $\mathrm{v}_i(t)$ and $a_i(t)$ are the instantaneous velocity and acceleration of the element at any arbitrary time t. It should be mentioned that $\mathrm{v}_i(t)$ and $a_i(t)$ are oscillatory in nature. Now, as seen from equation (10), $F_{\mathrm{lat},i}(t)$ consists of two components, lateral drag ($F_{\mathrm{v},i}$) as the fin undulates and inertial ($F_{\mathrm{a},i}$) force, which are given by the following equations, respectively

$$F_{\mathrm{v},i}\left(t\right) = \frac{1}{2}C_y\rho v_i(t)^2\Delta x\Delta z \tag{11}$$

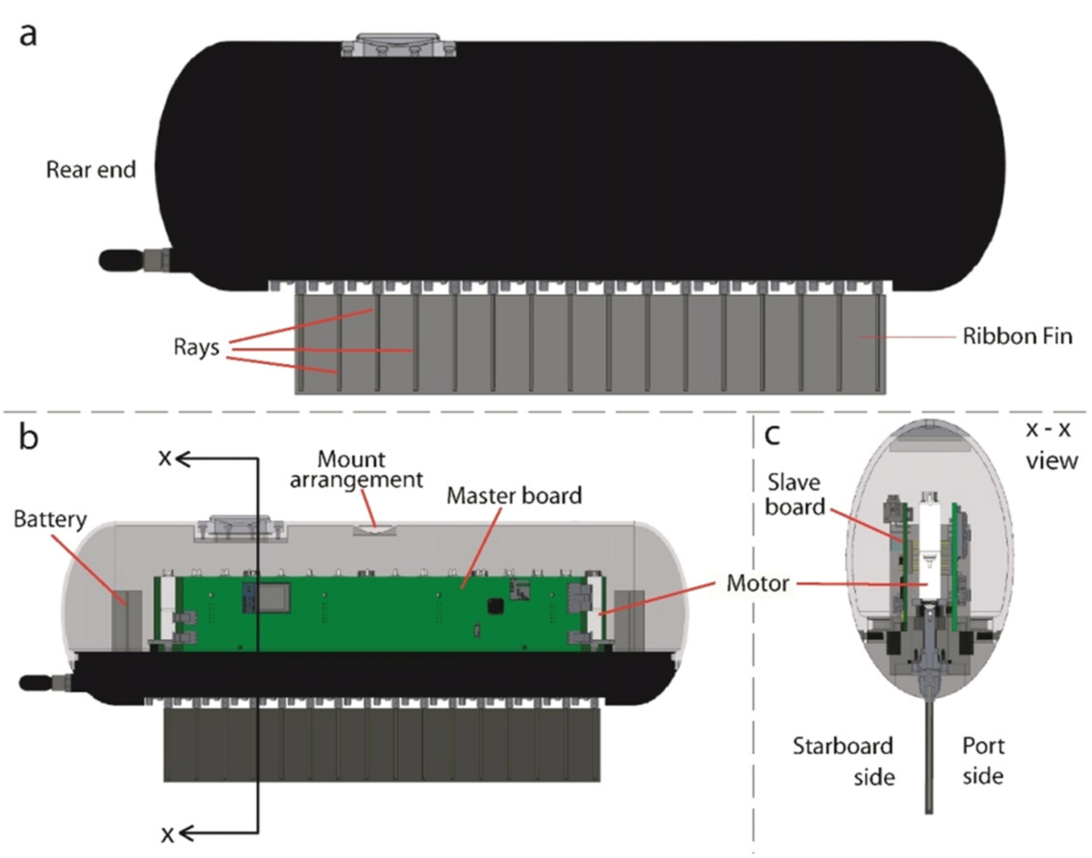

Figure 3. Schematic diagram of Knifebot. (a) Rendering showing the starboard view of the vessel. A flexible membrane is controlled with 16 rays independently actuated by 16 motors. (b) Rendering of the vessel with translucent top hull. (c) Cross section of the vessel. The vessel's hull houses two batteries (one in front and the other in the back of the vessel), electronic boards, motors. Two batteries, one at the front and one at the rear end of the vessel, deliver power to all the electronics during operation.

$$F_{a,i}\,(t) = M_{a,i}a_i(t) \tag{12}$$

C_y is the transverse force coefficient of the fin. For each element, the added mass was computed as

$$M_{a,i} = \frac{\pi}{4}\rho\Delta x\Delta z^2. \tag{13}$$

The total power required for lateral actuation of the fin is the sum of the power resulting from all the elements, and can be computed as follows.

$$P_{lat}\,(t) = \sum_{i=1}^{N} P_{lat,i}\,(t)\,. \tag{14}$$

As all forces being oscillatory, the final output power will also be a sinusoidal function. Thus, the effective lateral power is the root mean square value of the time series of lateral power:

$$\overline{P_{lat}} = \sqrt{\frac{1}{T}\int_0^T P_{lat}^2\,dt}. \tag{15}$$

Based on the estimated power, we calculate power efficiency in surge motion based on the useful power in surge (TU) and the total power (P_{tot}) as follows.

$$\eta = \frac{TU}{P_{tot}} = \frac{TU}{\overline{P_{lat}} + TU}. \tag{16}$$

3. Materials and methods

3.1. Robotic vessel

The robotic system (figures 2 and 3) is the second version of a vessel motivated by the black ghost knifefish [29, 32], a freshwater fish found in the Amazon basin and South America. The entire robotic vessel has a mass $M = 3.26$ kg. In this new version, the hull was built from aluminum (alloy 6061). The top hull is a watertight structure, encasing all the electronics. The propulsion system is located at the bottom of the hull, along the length of the vessel. This vessel provides an overall structural buoyancy of 3310 cm^3, that gives an equivalent upward mass force of 3.31 kg-force.

3.2. Hull

The aluminum hull consists of two portions, the upper and lower parts (figure 3(b)). The lower part houses sixteen motors, each of which actuates one ray that is located at the bottom of the vessel. When assembled, the hull is 44.3 cm long (L_{hull}), with a height of 13 cm (H_{hull}) and a maximum width of 7.8 cm at the constant parallel midship section. Radio frequency is used to communicate with the robotic vessel from the user station. Seals were provided by (1) one o-ring between the top and bottom parts of the hull, (2) shaft seals for each motor shaft and (3) an o-ring for the antenna cap.

Table 1. Experiments and parameters considered for: (1) fin force measurement, (2) drag measurements and (3) free swimming experiments.

Experimental configuration	Freq, f (Hz)	$\frac{L_{fin}}{\lambda}$	U (m s^{-1})	Re	Measurement
Fin force measurement exp.	0.5, 1	1, 2	0–0.1875	$0–8.3 \times 10^4$	F_{net}
Drag measurement exp.	—	—	0–0.7	$0–3.1 \times 10^5$	D_{hull}
Free swimming exp.	0.5, 1.0, 1.5, 2.0, 2.5, 3.0	1, 2	—	$0–1.77 \times 10^5$	U_{sw}

3.3. Electronics

The robotic fish is a self-contained robotic system with all the electronics, power source and communication on-board. Its electronic components consist of one main board, four motor controller boards, two batteries and 16 DC motors (RE10, Maxon Motor AG, Sachseln, Switzerland), everything accommodated inside the main hull (figure 3).

3.4. Propulsion

The propulsion system of the robotic fish is a stretchable fin membrane, located at the ventral side of the vessel (figures 2 and 3). As stated before, it consists of sixteen rays, each of them actuated by a motor located inside the hull. The elastic fin was made with a double layer of Lycra fabric 30 cm long (L_{fin}) and 7.7 high (H_{fin}). The two pieces of fabric were sewn together, providing pocket compartments to insert the rays. Extra membrane material between each ray allows for minimizing the stretching force needed when the rays are actuated. The motors were programmed such that the fin is capable of generating sinusoidal motion. In the present work, we focus mainly on the forward thrust force. The angular deflection of the mth ray, with $m = 1$ (first ray) to 16 (last ray), at time t is given by

$$\theta(m,t) = \theta_{max} \sin 2\pi \left(ft - \frac{L_{fin}}{(m-1)\lambda} \right) \quad (17)$$

f and λ are the frequency and wavelength of the fin wave, and $L_{fin} = 30$ cm is the length of the fin. Before conducting the experiments, the motors were accurately tuned so that each ray undulates in a sinusoidal wave with a maximum angular deflection of $\theta_{max} = 30°$.

3.5. Experiments

We conducted three different sets of experiments (table 1 and figure 4). For the first set, the net force generated by the fin was measured for varying fin frequency, wavelength, and flow velocities (figure 4(a)). For this experimental set, only the fin was submerged under the water, and we considered four different combinations of fin actuation: $f = [0.5, 1]$ Hz and $L_{fin}/\lambda = [1, 2]$ (we will refer to this parameter as the wave number). For all combinations, the flow velocity was varied from 0 to 0.1875 m s^{-1} with 0.0125 m s^{-1} increments, making the range of Reynolds number, $Re = L_{hull}U/\nu = [0–8.3 \times 10^4]$, where ν is the kinematic viscosity of the water. In the second set of experiments, the drag of the vessel (hull plus a straight fin without actuation) was measured for different velocities (figure 4(b)). In this experimental setup, the vessel was towed at different velocities using a carrier. Here we measured the drag force of the vessel as a function of Reynolds number. We considered towing speed in the range of 0.05 m s^{-1} to 0.7 m s^{-1}, this is $Re = [0.2–3.1] \times 10^5$. For the third experimental setup the free-swimming velocity of the vessel was measured for different fin actuations (figure 4(c)). In this experimental set the vessel was not tethered or mounted to any structure. We consider a combination of frequency between 0–3 Hz and $L_{fin}/\lambda = [1, 2]$.

3.6. Fin force measurement experiment

In order to perform a systematic investigation into the undulating fin force, we measured the force in the robotic fin for a range of wave velocities (V) and flow velocities (U), as shown in figure 4(a). This experiment was carried out in a flume 2 m long, with a cross sectional area of 25 cm × 25 cm. The flume was filled to 24 cm of its height. During force measurement experiments, the vessel was mounted in an air bearing system (New Way Air Bearings, Aston, PA, USA), such that the top edge of the ribbon fin is submerged in water; the rest of the body was kept outside in the air. Two precision metal rods with circular cross sections, each going through two mounting blocks, were firmly attached to rails along the flume. The housing plate was leveled thoroughly before and after the robotic vessel was mounted on it. The housing plate was attached to a horizontally mounted loadcell (Futek LSB-200, capacity: 1lb, FSH01559), with ±0.1% nonlinearity of rated output (±0.88 mN in measured force or approximately 0.092 g of force). The load cell was calibrated with the same experimental setup before conducting the experiments. As shown in table 1, we conducted four different sets of experiment. During each set, the undulating fin in the robotic vessel was actuated at a fixed value of frequency and period, resulting in a fixed wave velocity (V) in the fin. Each set considered 16 experimental runs. For each experimental run, we took zero readings from the loadcell for 10 s, followed by 30 s data acquisition at a sampling rate of 1000 Hz. Before recording each time series, we let enough timeelapse (approximately 30 s) to prevent the initial transient condition.

Note that the experimental force represents the net force of the fin, $F_{net} = T - D_{fin}$. To obtain the thrust generated by the fin, we estimated the drag at

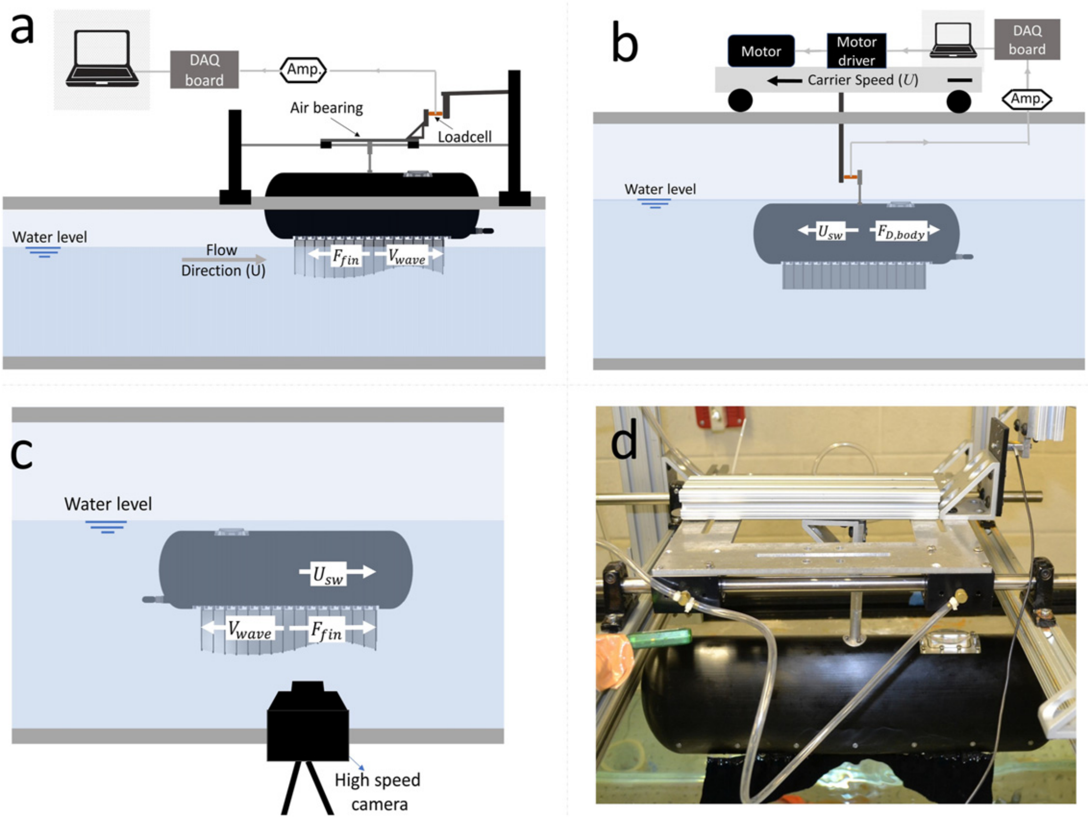

Figure 4. Experimental setups for fin force measurement (a), body-fin drag measurements (b) and free-swimming experiments (c). (a) Schematic for the fin force measurement experiment. In this set of experiments only the fin was submerged in the water. The vessel was supported with an air bearing system that was attached to a unidirectional load cell. (b) Schematic for body drag measurement experiment. The submerged vessel was mounted in a carrier with the fin straight without actuation. (c) Schematic of the free-swimming experiments. The vessel was free-swimming along the centerline of the water tank without flow motion. (d) Picture of the experimental setup for the fin force measurements.

the condition when $U = V$, that is, when the incoming flow is equal to the wave speed. Under this condition, both models agree that the thrust is equal to zero (equations (5) and (6)).

3.7. Drag force characterization experiment

The drag of the vessel was measured for different towing velocities, through a water tank (18 m long × 1.2 m wide and water depth 0.45 m). The tank is equipped with a motor-driven carrier that can run along the length of the tank. The speed and acceleration of the carrier can be programmed and controlled by a programmable indexer software (SMC60WIN by Anaheim Automation—version 2.01). During the experiment, the robotic vessel was mounted on the carrier through a load cell (Futek LSB-200, capacity: 1lb, FSH01559), previously calibrated under the same conditions as the experiment. While conducting these experiments, the fin was left idle. The carrier motor was programmed to tow the robotic fish at a constant speed. Each experiment reading was 4 s long, at a sampling rate of 1000 Hz. The drag coefficient of the vessel is given by

$$C_D = \frac{D_{hull}}{\frac{1}{2}\rho A_p U^2}. \tag{18}$$

Due to the very small cross sectional area of the fin, we neglect the frontal area of the fin.

3.8. Free-swimming experiment

Finally, the free-swimming speed, U_{sw}, of the robotic vessel was measured for different fin actuations. We varied the frequency (f) and wavelength (λ) of the sinusoidal motion in the fin and measured the free-swimming velocity of the vessel (figure 4(c)). These experiments were conducted in the same water tank as the hull drag measurements, with a length, width and water depth of 18 m, 1.2 m and 0.45 m, respectively. A high-speed camera (Photron FASTCAM Mini UX 50, Tokyo, Japan) was set up beside the tank to record the swimming motion at 50 frames per seconds. Three white markers located at the port side of the vessel, shown in figure 2(b), were used to track the vessel after the recording was conducted. The robot was released to swim through the midsection of the tank. Before each run, it was ensured that the water was calm before releasing the vessel. The recorded video was later post processed with MATLAB (version 2019b) to track each of the three markers on the vessel, from which we estimated the free-swimming velocity. The resolution of the camera (1280 × 1024 pixels) translates for the motion tracking results in a resolution of 0.753 mm/pixel.

The experimental data for the three experiment sets were filtered using a low-pass filter with a cut-off frequency of 2 Hz. The standard deviation of the

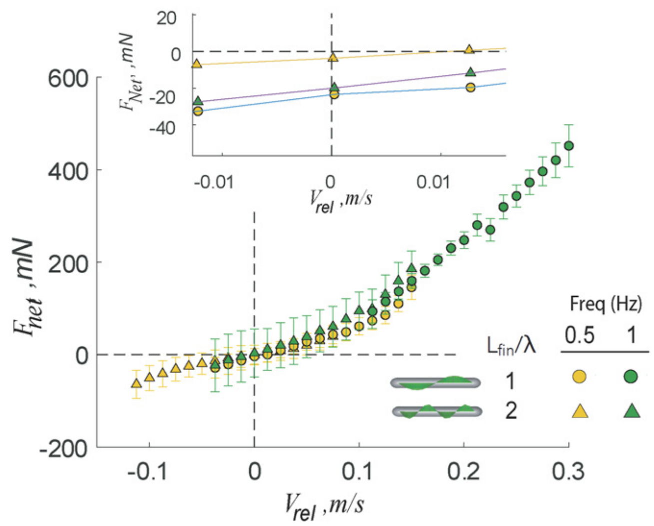

Figure 5. Experimental net fin force plotted against relative velocity, V_{rel}. The inset shows a zoom-in view of the main plot when $V_{\mathrm{rel}} = 0$.

processed data was computed to show the variation of the measured readings. The standard deviations are shown in figures 5, 10 and 11 as error bars.

4. Results and discussion

4.1. Experimental fin force and propulsive efficiency

The net force generated by the fin, F_{net}, increases with the relative velocity, V_{rel}, for all cases. As described in the material and method section, the drag of the fin while undulating was estimated as the net force intercept when $V_{\mathrm{rel}} = 0$ (inset figure 5). D_{fin} was equal to [3.6, 20, 23.5] mN for ($f = 0.5$ Hz, $\frac{L_{\mathrm{fin}}}{\lambda} = 2$), ($f = 1$ Hz, $\frac{L_{\mathrm{fin}}}{\lambda} = 2$) and ($f = 0.5$ Hz, $\frac{L_{\mathrm{fin}}}{\lambda} = 1$), respectively. For ($f = 1$ Hz, $\frac{L_{\mathrm{fin}}}{\lambda} = 1$) there was no intercept. We estimated $D_{\mathrm{fin}} = 20$ mN as the data follows closely the second case ($f = 1$ Hz, $\frac{L_{\mathrm{fin}}}{\lambda} = 2$).

Figure 6 shows the experimental thrust force generated by the fin ($T = F_{\mathrm{net}} - D_{\mathrm{fin}}$). As can be observed in figure 6(a), there is a monotonic decrease in the thrust force, T, as the incoming flow speed increases for all the fin kinematics tested. It is also evident that the thrust force is highly dependent on the incoming flow. Figures 6(b) and (c) depict the thrust force as a function of ($V^2 - U^2$) and relative velocity ($V - U$), respectively.

From figure 6(a), it is evident that T has a strong dependency on flow velocity around the fin. However, the datasets are scattered, failing to follow a common curve. Therefore, U could not be considered the characteristic velocity for the thrust force. In figure 6(b), two cases are found to be collapsing into the same trend (green triangles and yellow circles). These two cases have equal wave velocity, $V = 0.15$ m s^{-1}. However, the other two datasets exhibit an offset in the thrust. In figure 6(c), we observe that all the datasets seem to follow a common behavior following a narrow band for the thrust generated by the fin.

Figure 6(d) plots the natural log of the force, $\log_e(T)$, along the vertical axis, against the natural log of V_{rel}, $\log_e(V_{\mathrm{rel}})$, along the abscissa. A slope of 2 is shown for reference. Note that a linear relationship in the log–log plot indicates a power relation between the quantities associated with the slope of the line. As seen in this figure, the slope of each dataset is close to 2. In this case, as previously reported [28], the thrust force T seems to scale proportionally to ${V_{\mathrm{rel}}}^2$.

4.2. Normalized fin force

Figure 7 shows the normalized thrust force plotted as a function of U/V. For any given fin actuation (f, $\lambda =$ constant), the normalized thrust force is the ratio between thrust force at a given flow velocity and thrust force at zero incoming flow. In this graph, all the experimental data are shown in circle and triangle symbols, in addition to the two different models for the thrust force—model 1: $T \propto V^2 - U^2$ (dashed line) and model 2: $T \propto (V - U)^2$ (solid line). The two vertical dashed lines show typical U/V values for the robotic vessel during free swimming (details in section 3.5) and reported for the knifefish [37].

For models 1 and 2, the thrust forces, when there is no flow, are given by the following expressions

$$T_{\mathrm{o},1} = C_k V^2 \tag{19}$$

$$T_{\mathrm{o},2} = \frac{1}{2} C_x \rho A_{\mathrm{e}} V^2. \tag{20}$$

Combining equations (5), (6), (19) and (20), the normalized thrust force for models 1 and 2 can be expressed respectively, as follows

$$\frac{T_1}{T_{\mathrm{o},1}} = 1 - \frac{U^2}{V^2} \tag{21}$$

$$\frac{T_2}{T_{\mathrm{o},2}} = \mathrm{sign}\,(V - U)\left(1 - \frac{U}{V}\right)^2. \tag{22}$$

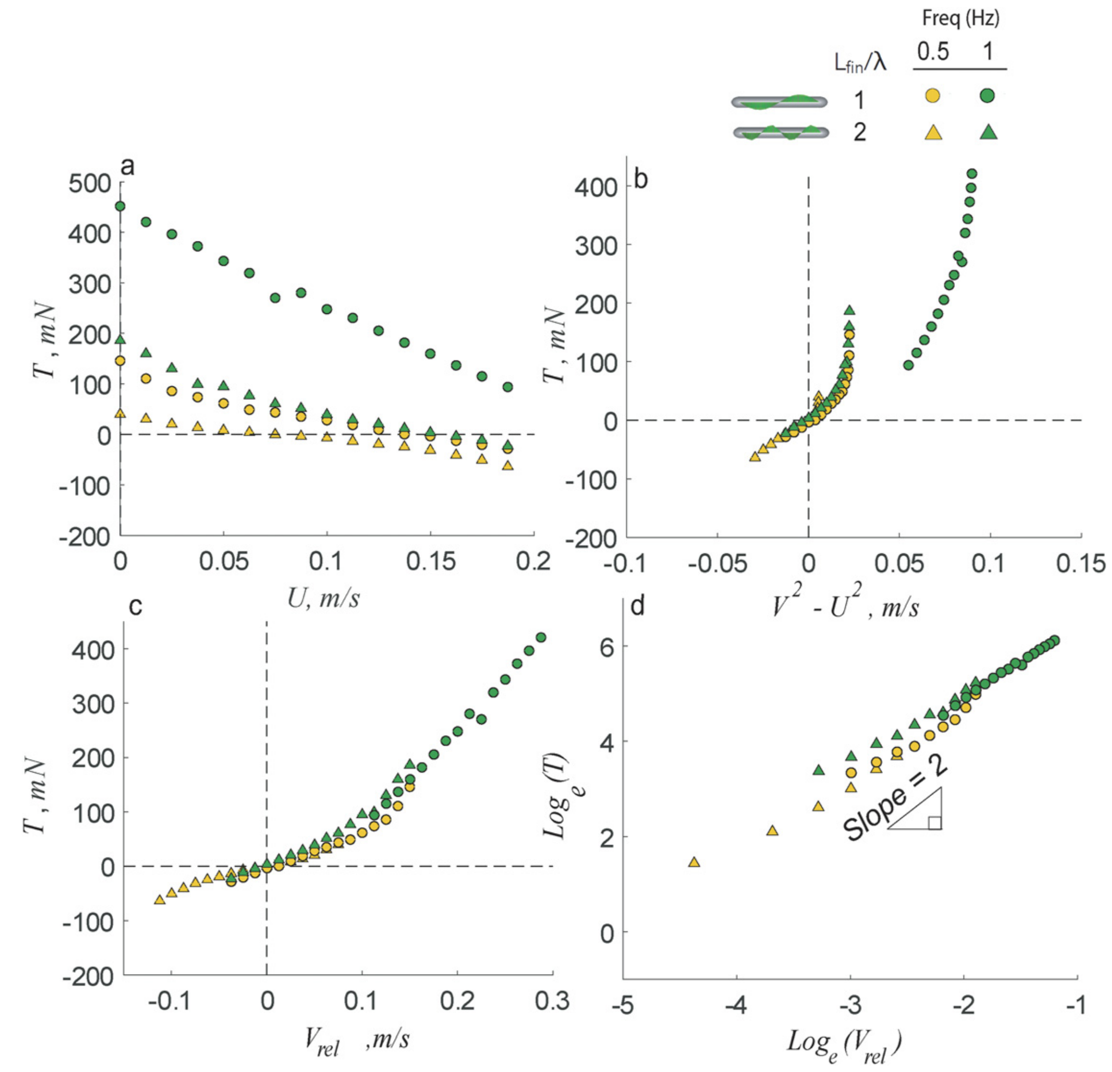

Figure 6. Experimental thrust generated by the fin. (a) Experimental thrust force versus flow velocity, (b) thrust force against $(V^2 - U^2)$. (c) Thrust force versus relative velocity $(V-U)$. (d) $\text{Log}_e(T)$ plotted against $\log_e(V_{rel})$. As a reference, a slope equal to 2 is shown. Wave number, $L_{fin}/\lambda = 1$ and 2 are shown as circle and triangle symbols. Frequencies of 0.5 and 1 Hz are shown with yellow and green symbols.

Here, sign $(V - U)$ takes a value equal to $+1$ when $V > U$, and yields -1 when $V < U$. Equations (21) and (22) were used to generate the force models (dashed and solid lines) in figure 7. The normalized fin force is a function of the ratio between swimming velocity and wave velocity in equations (21) and (22). Both models concurred that the maximum thrust force occurs when the U/V is equal to zero, and the thrust force is equal to zero when $U/V = 1$.

However, the trends of both graphs between these two points are very different. In the case of model 2, the thrust force approaches zero in an asymptotic manner as U/V tends to 1, while model 1 does not. The reverse happens when U/V tends to 0, where there is a sudden decrease in the thrust force in model 2 when U/V increases from the zero value. That can be demonstrated by the derivative of equations (21) and (22)

$$f'\left(U/V\right) = \begin{cases} -2U/V, \text{model1} \\ \text{sign}\left(V - U\right) 2(U/V - 1), \ \text{model2} \end{cases} \tag{23}$$

where $f'(U/V)$ is the derivative of T/T_o (for model 1 or model 2). When the derivative (the slope in figure 7) is evaluated at $U/V = 0$ the slope is equal to 0 and -2 for models 1 and 2, respectively. On the other hand, when evaluated at $U/V = 1$, the derivatives are -2 and 0 for models 1 and 2, respectively. A slope of 0 means the curve is asymptotically approaching at that point, whereas a slope of -2 means T/T_o undergoes a sudden decrease with the increase of U/V. The experimental data follows a common behavior in a similar fashion to model 2, with a sudden decrease in thrust force (T/T_o) when U/V is increased from zero, and asymptotically approaches zero when U/V tends to 1.

From figure 7, it is clear that the correlation between model 2 and experimental data exists through a large range of U/V. On the other hand, a

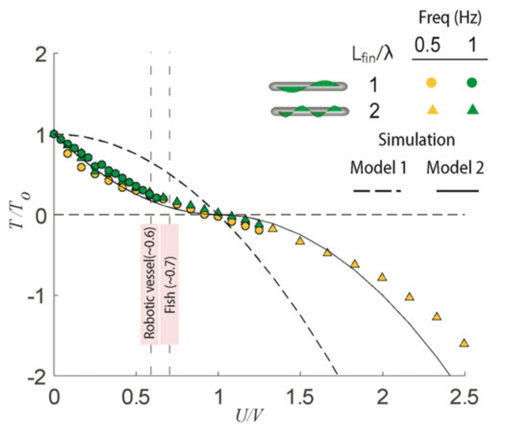

Figure 7. Comparison between force models and experimental data. Experimental data are shown with symbols (circles and triangles) color coded for frequency. Simulations using model 1 are shown with a dashed black line and simulations for model 2 are shown with a solid black line. The swimming speed relative to wave speed for the robotic vessel and knifefish are shown with vertical dashed lines.

considerable difference is observed between model 1 and the experimental results. Moreover, near the two vertical dashed lines, where the robotic fish and knifefish operate, the experimental results closely agree with model 2.

4.3. Propulsive efficiency

Figure 8(a) shows the computed thrust force of the undulating ribbon fin normalized by the thrust force when there is no incoming flow. This normalized thrust force is shown by the blue symbols, and it is based on model 2 (equation (22)). In addition, figure 8(a) shows the hydrodynamic efficiency plotted with red symbols based on equation (16). The efficiency, as described before, is based on the total lateral power (added mass + pressure force) plus the power in the surge direction (TU). The propulsive efficiency for undulating bodies (equation (4)) is shown with a gray dashed line for reference.

Figure 8 focuses on the region for U/V between 0 and 1 that is more relevant for swimming animals and underwater vehicles. Wavelength is shown with the circle and triangle symbols. The normalized thrust force starts at 1 when there is no incoming flow ($U/V = 0$) and starts to quickly decay, approaching 0 in an asymptotic manner as U/V approaches 1.

For the case of the propulsive hydrodynamic efficiency (red symbols), it starts from zero, as the swimming speed is equal to zero. Under this condition, even though the fin is generating the maximum force, the fin is stationary ($U = 0$), therefore there is no useful power. As U/V increases, the efficiency also increases until it peaks, and then starts to decay. When U/V is equal to 1 the efficiency goes back to zero as there is no thrust force ($T = 0$) generated by the fin. That means that the fin could not provide any thrust force to propel a body (main source of drag). This behavior in the efficiency of undulating fin propulsion, resembles the trend of the performance curve of traditional propellers if we compare U/V to the advance ratio in propellers (U/tip velocity). In this regard, undulating ribbon fin propulsion is rather different to an undulating body, as it has a highly decoupled source of thrust and drag. As a reference, the efficiency for undulating bodies or wave planes is shown with a dashed line in figure 8(a). There are some clear limitations with this efficiency model for undulating fin propulsion. First, it tends to 50% efficiency when the swimming velocity approaches zero, and the efficiency goes to 100% when $U/V = 1$.

The peak efficiency is highly dependent on the wavelength (figure 8(a) red triangles and red circles), as higher efficiency occurs for large wavelength. The efficiency decreases by approximately 63% when L_{fin}/λ is changed from one to two wavelengths. Note that when using this modelling, the efficiency does not depend on the frequency. However, the efficiency could change with the stretch force of the fin.

Figure 8(b) shows the efficiency for two different ratios between lateral and thrust force coefficients (C_y/C_x). The efficiency was computed when the proportions are equal, $C_y/C_x = 1$, and when $C_y/C_x = 3.8$. This proportion of the force coefficient could be highly impacted by the fin material as well as flow conditions. Thus, these two curves represent a potential range of the fin efficiencies. The peak efficiency of the modeled undulating fin was 0.754 for $U/V = 0.33$. However, there is a relatively wide range of U/V where the performance is relatively close to the peak performance. The gray region shows the efficiencies that are more than 90% of the maximum efficiency.

4.4. Swimming speed relative to wave speed, U/V

An important relationship that can be established using the equation of motion (equation (9)) is U/V—the quasi-steady state swimming speed relative to the wave speed. After the initial acceleration has passed ($\ddot{x} = 0$), using the model for thrust force and body drag (equations (6) and (8), respectively) and assuming that $D_{\text{hull}} \gg D_{\text{fin}}$, it can be derived that

$$\frac{U}{V} = \frac{1}{1 + \sqrt{\frac{A_p}{A_e}\frac{C_D}{C_x}}}. \tag{24}$$

It is interesting to note that U/V depends only on two ratios: (1) the ratio between the projected body area to fin-swept area (A_p/A_e), and (2) the ratio between body drag coefficient to fin propulsive coefficient (C_D/C_x).

Figure 9 shows the computed swimming speed normalized by the wave speed, (U/V), using blue symbols. This normalized swimming speed is calculated using equation (24). The graph shows how the normalized swimming speed changes for different A_p/A_e ratios. In addition, two simulations were considered with different ratios between the coefficient

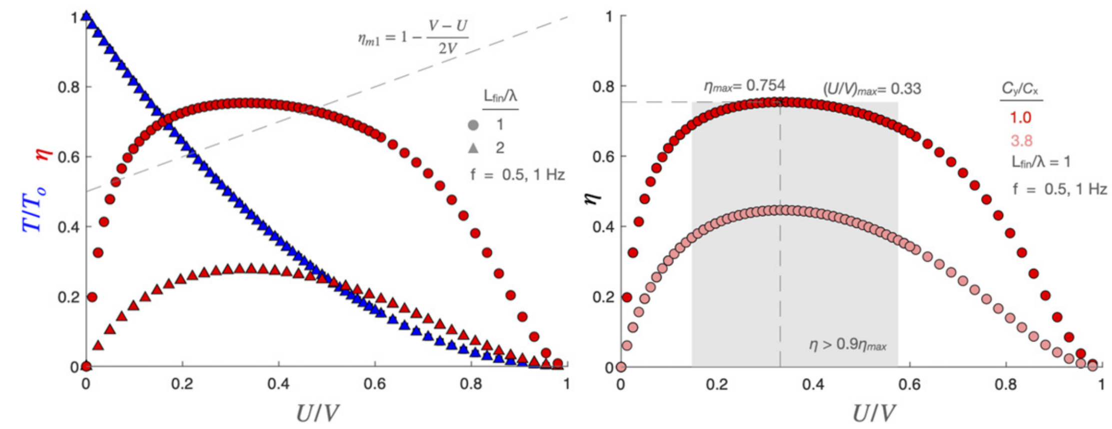

Figure 8. (a) Propulsive efficiency (red) and normalized fin force (blue) versus velocity ratio (U/V). Circular and triangular symbols show the results for one and two wave numbers. The gray dashed line shows the propulsive efficiency from previously proposed propulsive efficiency for undulating bodies η_{m1} [22, 24]. (b) Propulsive efficiency versus U/V for two different ratios of lateral to forward coefficient of force (C_y/C_x) for $L_{\text{fin}}/\lambda = 1$ and $f = [0.5, 1]$ Hz. The vertical and horizontal dashed lines show the location of the peak efficiency. The gray area shows the region where the propulsive efficiency is equal to or greater than 90% of the maximum propulsive efficiency.

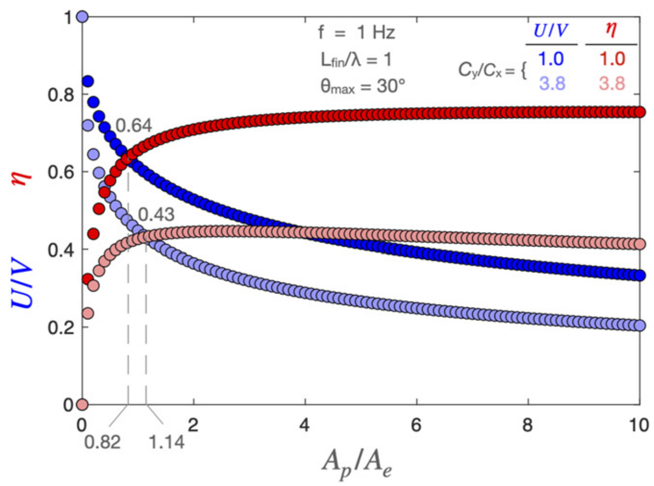

Figure 9. Computed swimming speed normalized with wave speed, U/V (blue circles), and propulsive efficiency (red circles) as a function of the ratio of body frontal area to swept area, $A_{\text{p}}/A_{\text{e}}$. The fin kinematics were constant, as well as the swept area, A_{e}. Two C_y/C_x were considered: 1 (dark red and dark blue) and 3.8 (light red and light blue). The intercept between U/V and efficiency for both cases are shown with dashed lines.

of force for the longitudinal direction (C_x) and lateral direction (C_y). The dark and light blue are for $C_y/C_x = [1, 3.8]$, respectively. For these computations, the fin kinematics were constant: $L_{\text{fin}}/\lambda = 1$, $f = 1$ Hz and $\theta_{\text{max}} = 30°$, as well as the fin geometry $L_{\text{fin}} = 30$ cm and $H_{\text{fin}} = 7.7$ cm. The drag coefficient was taken as $C_{\text{D}} = 0.76$ (see figure 10). This plot considers $C_x = 0.5$ based on the average force measurements (figure 6). The difference between the dark and light blue can be interpreted as an uncertainty dependent on the C_y/C_x ratio.

The $A_{\text{p}}/A_{\text{e}}$ ratio was changed by changing A_{p} (the frontal projected body area). When there is no body ($A_{\text{p}}/A_{\text{e}} = 0$), $U/V = 1$ (that is, the swimming speed is equal to the wave speed). At the beginning, as the $A_{\text{p}}/A_{\text{e}}$ increases (increasing the body area), there is a sharp decrease in U/V. U/V keeps decreasing with increasing $A_{\text{p}}/A_{\text{e}}$ but at a lower rate.

Figure 9 also shows the computed hydrodynamic efficiency for the two cases, $C_y/C_x = [1, 3.8]$, in dark and light red, respectively. The hydrodynamic efficiency is based on equation (16). The difference between these two curves can be represented as an uncertainty dependent on the ratio of force coefficients between lateral and forward force. In the case of propulsive efficiency, efficiency starts from zero when $A_{\text{p}}/A_{\text{e}} = 0$, which means that there is no thrust generated to propel a body. Then, as $A_{\text{p}}/A_{\text{e}}$ increases, there is first a sudden increase in the efficiency, followed by a plateau region. For large $A_{\text{p}}/A_{\text{e}}$, it is expected that the efficiency decreases again. For the two different C_y/C_x ratios, as the C_x decreases compared to the C_y (that is, higher C_y/C_x), both the U/V and efficiency decreases. As expected, this decrease in efficiency is because the ability to generate thrust force diminishes while the power related to lateral fin motion remains the same.

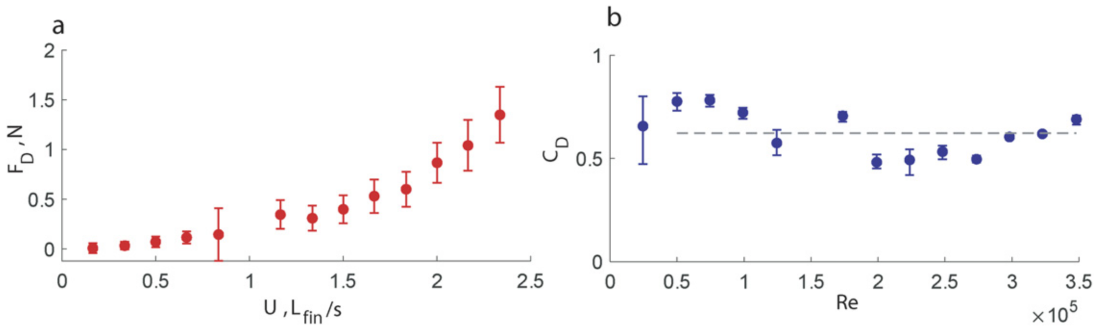

Figure 10. Experimental results from body drag. (a) Time average body drag versus speed. (b) Drag coefficient versus Reynolds number based on the length of the hull.

From this graph we can observe that animals or underwater vehicles using this type of propulsion will have to do a trade-off between speed and efficiency. High speed compared to wave speed (that is, high U/V) will tend to have a low efficiency while high efficiency will result in swimming at moderate speed compared to wave speed. In the graph, the intercept between efficiency and speed is shown with dashed lines for both cases. The intercepts are 0.64 for $A_p/A_e = 0.82$ ($C_y/C_x = 1.0$) and 0.43 for $A_p/A_e = 1.14$ ($C_y/C_x = 3.8$). It is possible that a compromise is made around this intercept to balance both speed and efficiency (this will be commented on further in the section *implications for biological swimmers)*.

4.5. Hull drag characterization

Figure 10(a) shows the variation of mean body drag with respect to speed. Drag force undergoes nonlinear monotonic increase with U. It should be noted that, in addition to the drag of the hull of the vessel, F_D includes the drag due to upright idle fin.

In figure 10(b), the nondimensional drag coefficient (C_D) is plotted against Reynolds number (Re), considering the length of the hull (44.3 cm) as the characteristic length. The error bars correspond to standard deviation of the measurements. The expression to calculate Reynolds number is given by

$$\mathrm{Re} = \frac{UL_{\mathrm{hull}}}{\nu} \qquad (25)$$

where ν is the kinematic viscosity of water. For most cases, the drag coefficient is independent of Reynolds number, and except for a few data points, the calculated drag coefficient remains approximately the same. The horizontal dashed line in figure 10(b) shows the average drag coefficient, $C_{D,\mathrm{mean}} = 0.76$ for all points except the first point on the left of the plot. In previous studies, Curet *et al* [28] showed that the drag coefficient for the upright fin can vary between 0.02–0.03. This means that the drag coefficient for the hull of the robotic vessel would be slightly smaller ∼0.73–0.76.

4.6. Free-swimming experiment

The results of free-swimming experiments are shown in figure 11. In each graph the experimental results are shown with circle and triangle symbols for wave numbers 1 and 2, respectively. The symbols are also color coded for the fin frequency (light yellow 0.5 Hz to dark red 3 Hz). In addition, the computed steady-state swimming velocities are shown with solid light and dark blue for $L_{fin}/\lambda = [1, 2]$, respectively, based on equation (24). As before, here we consider $C_x = 0.5$, $C_D = 0.76$ and $\theta_{max} = 30°$. Figure 11(a) shows the variation of the swimming velocity (U_{sw}) of the vessel with wave speed (V), which has a unit of L_{fin}/s ($1L_{fin}/s = 0.3$ m s^{-1}). For the most part, experimental results exhibit a linear relationship between swimming speed and wave velocity. For higher frequencies (2.5 and 3 Hz) when the wave number is 1, the swimming velocity was lower than the expected linear relationship. This decrease in speed has also been exhibited in other robotic systems with undulating fin propulsion [31]. For the case that $L_{fin}/\lambda = 2$, all experimental results for swimming velocity follow a linear relationship with the wave speed. The computed swimming velocities are in very close agreement with experimental data. This close estimate of the swimming velocity further validates the model for the thrust generated by the fin under free-swimming conditions. Figure 11(b) shows the Strouhal number, St $= fA/U_{sw}$, where A is the peak-to-peak amplitude at the mid-fin height. For the case of $L_{fin}/\lambda = 1$, the Strouhal number for simulation is approximately 0.2, which is reflected for most of the experimental cases as well. However, for low and high frequencies, St tends to increase. $L_{fin}/\lambda = 1$ had the better efficiency performance, and it does agree with the range of St = 0.2–0.3 for optimal swimming. For $L_{fin}/\lambda = 2$ the Strouhal number increases to 0.4 for both experiments and simulations. For the experimental data at low frequencies, St tends to increase.

Figure 11(c) shows the free-swimming speed normalized by the wave speed, U_{sw}/V, as a function of U_{sw}. As previously mentioned in the modeling section, U/V is independent of frequency or wavelength. For both cases, in simulation and experiment, the U/V is approximately 0.6. The experimental results for free-swimming are in close agreement, only

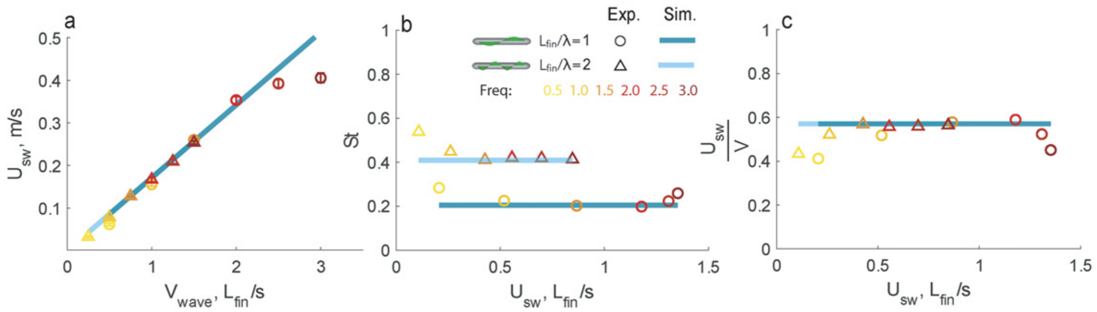

Figure 11. Experimental results and simulations for free-swimming conditions. (a) Swimming speed, U_{sw}, versus wave speed. (b) Strouhal number vs swimming speed. (c) U_{sw}/V vs U_{sw} Experimental results are shown with circle and triangle symbols for $L_{fin}/\lambda = [1, 2]$, respectively. The experimental symbols are color coded with frequency of fin oscillation. Simulations are shown in solid blue and light blue for wave numbers 1 and 2. The symbols are color coded with the fin frequency.

the case for very low swimming speed or high swimming speed are below the expected ratio. Thus, for a given hull body (fish body) and fin geometry with a single traveling wave, to change U/V will require a change of swept area (A_e) through a change in the maximum amplitude of oscillation.

5. Implications for biological and engineered swimmers

The results from this work have multiple implications for both biological swimmers and the design of engineered underwater vehicles with undulating ribbon fin propulsion.

5.1. Thrust

Direct thrust force measurements in biological swimmers are particularly difficult or impossible to perform. Thus, physical models, computational and theoretical work are essential to understand how thrust changes with different parameters such as fin kinematics or flow speed. In this work, a thrust model for undulating fin propulsion was tested against experimental data using an undulating robotic system for different actuation parameters and flow conditions. The experimental data support that thrust is proportional to the square of the relative velocity between the incoming flow and the wave speed, that is, $T \propto (V - U)^2$. This result was tested with a systematic change of flow and changing wave speed with fin frequency and wavelength ($V = f\lambda$). Having an empirically tested force model is very valuable to then estimate thrust for live animals and for the design of underwater vehicles using undulating fin propulsion. Moreover, the thrust force model can be used to estimate swimming speed and the propulsive efficiency.

We found that thrust has a high dependency on the ratio between the free stream flow, U, and wave speed, V. For live animals or vessels freely swimming in stagnant water, U will represent the swimming speed. There is a steep decrease in thrust as the swimming speed increases from zero and the wave speed is held constant. Then, thrust approaches zero when $U/V \sim 1$. This underlines one of the trade-offs that any vessel or live animal with an undulating fin must deal with; to achieve high speeds compared to the wave speed, only a limited thrust will be generated. Thus, if speed is an important factor in the swimming performance, this would require streamed body forms as well as limits in the frontal area. These features are exhibited in fishes using undulating fin propulsion such as knifefish.

5.2. Efficiency

Hydrodynamic efficiency curves were computed based on thrust, free-stream flow, and lateral fin forces. The efficiency curves versus U/V exhibits an inverse 'U' shape with zero efficiency at $U/V = 0$ and $U/V = 1$, and a maximum efficiency of around 0.75 when U/V is approximately 0.33. Although the exact shape of the efficiency curve and maximum efficiency most likely will depend on the fin membrane material and its geometry, it should exhibit a similar trend with a peak value. This efficiency curve is very different from the efficiency proposed for undulating bodies. One of the main differences is that the drag source and propulsion in an undulating fin-propelled system are highly decoupled. Therefore, an undulating fin as a propulsive mechanism has to propel a body that would be the main source of drag, not only to transport the fin itself. Moreover, in undulating ribbon fin propulsion the fin kinematics is accompanied by a rotation of the fin as opposed to an undulating body or a wavy plate where the motion is in one plane. This rotation would have a significant impact on the 3D features of the flow structure and potentially its efficiency and force characteristics.

It is interesting to note that even though we observe a peak value of the hydrodynamic efficiency (figure 7), there is a broad range where the fin operates very close to the peak efficiency. This characteristic of the fin efficiency would allow a biological or engineered system to change its operational U/V speed around that peak value and still be close to the peak efficiency.

Another important aspect is that high efficiency occurs at longer wavelengths. Of course, variation of the number of waves along the fin will also affect the net lateral forces and thus the oscillation motion.

5.3. Swimming speed relative to wave speed, U/V

An expression for swimming speed relative to wave speed has been presented (equation (24)). This normalized swimming speed only depends on two ratios: the projected body area to fin-swept area (A_p/A_e) and the body drag coefficient to propulsive fin force coefficient (C_D/C_x). We can note that if the maximum fin amplitude is constant, the U/V will be in general a constant value, independent of the wavelength or fin frequency. If the thrust force coefficient and drag coefficient are constant (in many cases they are), for a given body and fin, the only way to change the U/V ratio would be the changing of the swept area which could be done by modulating the amplitude of deflection. This U/V equation can be used to indirectly estimate the thrust coefficient in live animals as well. A_e is a geometrical parameter that can be estimated from swimming kinematics along with the swimming speed and wave speed. In addition, A_p can be measured from the body morphology. It is also possible to measure the drag coefficient of the body or estimate it from similar body shapes. Then, the thrust coefficient could be solved from equation (24).

Previous work has suggested an increase in thrust when an undulating fin is attached to a rigid body compared to the fin undulating by itself, which has been referred to as momentum enhancement. This momentum enhancement was used to explain the common ratio of body length to body-fin length exhibited in undulating fin swimmers [3]. However, recent work using a physical model shows a lack of momentum enhancement [34]. Thus, it is still unclear as to why this similar body-to-fin-length ratio occurs in natural swimmers. Based on this work, we can hypothesize that there could be a trade-off between swimming speed and efficiency that results in a compromise between the body size and fin height. We suggest that the intersection between efficiency and U/V could be explored to explain the body and body-fin length ratio found in natural swimmers.

6. Conclusion

Biological swimmers with undulating ribbon fin propulsion can exhibit impressive maneuvers. A force scaling and performance analysis of this propulsion system could allow us to understand better the capabilities of biological swimmers as well as the design of engineered systems inspired by undulating fin propulsion. In this work, we presented a thrust scaling and efficiency analysis of undulating fin propulsion based on empirical force measurements and force modeling. Using a robotic vessel with an undulating fin propulsion, three sets of experiments were performed: (1) measurements of thrust as the incoming flow was systematically varied; (2) body drag measurements; (3) measurements of free-swimming speeds. It was found that the thrust force measurements follow a scaling of $T = 0.5C_x\rho A_e(V - U)|V - U|$ where C_x is the thrust force coefficient and $(V - U)$ is the relative velocity between the wave speed and incoming flow speed. Furthermore, a hydrodynamic propulsive efficiency based on this empirical thrust force and lateral power model for the fin, were computed for different U/V ratios and force coefficients. It was found that the propulsive efficiency exhibits a broad high performance versus U/V with a maximum efficiency of 0.754 for $C_y/C_x = 1$ and $L_{\text{fin}}/\lambda = 1$. An expression to calculate swimming velocity over wave speed was presented. Our results were used to estimate the free-swimming velocity. In addition, the results were discussed in relation to their implications for both biological and engineered swimmers. Finally, it was suggested that the ratio of fin to body length could be due to a trade-off between swimming efficiency and swimming speed.

Acknowledgment

This material is based upon work supported by the National Science Foundation under Grant No. (#1751548) to OMC.

Data availability statement

The data that support the findings of this study are available upon reasonable request from the authors.

ORCID iDs

Oscar M Curet https://orcid.org/0000-0002-3202-6841

References

[1] Curet O M, Patankar N A, Lauder G V and MacIver M A 2011 Aquatic manoeuvering with counter-propagating waves: a novel locomotive strategy *J. R. Soc. Interface* **8** 1041–50

[2] Liu H, Gong F and Curet O 2017 Unleashing the potential of undulating fin propulsion using a biomimetic robotic vessel *Mar. Technol. Soc. J.* **51** 79–93

[3] Blake R W 1983 Swimming in the electric eels and knifefishes *Can. J. Zool.* **61** 1432–41

[4] Jagnandan K and Sanford C P J 2013 Kinematics of ribbon-fin locomotion in the bowfin, Amia calva *J. Exp. Zool.* A **319** 569–83

[5] Borazjani I and Sotiropoulos F 2010 On the role of form and kinematics on the hydrodynamics of self-propelled body/caudal fin swimming *J. Exp. Biol.* **213** 89–107

[6] Khalid M, Wang J, Akhtar I, Dong H, Liu M and Hemmati A 2021 Larger wavelengths suit hydrodynamics of carangiform swimmers *Phys. Rev. Fluids* **6** 073–101

[7] Khalid M, Wang J, Dong H and Liu M 2020 Flow transitions and mapping for undulating swimmers *Phys. Rev. Fluids* **56** 063104

[8] Khalid M S U, Wang J, Akhtar I, Dong H, Liu M and Hemmati A 2021 Why do anguilliform swimmers perform undulation with wavelengths shorter than their bodylengths? *Phys. Fluids* **33** 031911

[9] Youngerman E D, Flammang B E and Lauder G V 2014 Locomotion of free-swimming ghost knifefish: anal fin kinematics during four behaviors *Zoology* **117** 337–48

[10] Ayancik F, Zhong Q, Quinn D B, Brandes A, Bart-Smith H and Moored K W 2019 Scaling laws for the propulsive performance of three-dimensional pitching propulsors *J. Fluid Mech.* **871** 1117–38

[11] Fish F E 2020 Advantages of aquatic animals as models for bio-inspired drones over present AUV technology *Bioinspiration Biomimetics* **15** 025001

[12] Liu G, Ren Y, Zhu J, Bart-Smith H and Dong H 2015 Thrust producing mechanisms in ray-inspired underwater vehicle propulsion *Theor. Appl. Mech. Lett.* **5** 54–7

[13] Zhu J, White C, Wainwright D, DiSanto V, Lauder G and Bart-Smith H 2019 Tuna robotics: a high-frequency experimental platform exploring the performance space of swimming fishes *Sci. Robot.* **4** 1–12

[14] Smits A 2019 Undulatory and oscillatory swimming *J. Fluid Mech.* **874** P1

[15] Quinn D B, Lauder G V and Smits A J 2014 Scaling the propulsive performance of heaving flexible panels *J. Fluid Mech.* **738** 250–67

[16] Yu Y-L and Huang K-J 2021 Scalling law of fish undulatory propulsion *Phys. Fluids* **33** 061905

[17] Hu Q and Yu Y 2021 Hydrodynamic scaling law in undulatory braking locomotion *Sci. China Phys. Mech. Astron.* **64** 274711

[18] Buren T, Floriyan D, Wei N and Smits A 2018 Flow speed has little impact on propulsive characteristics of oscillating foils *Phys. Rev. Fluids* **3** 013103

[19] Van Buren T, Floryan D and Smits A J 2019 Scaling and performance of simultaneously heaving and pitching foils *AIAA J.* **57** 3666–77

[20] Floryan D, Van Buren T and Smits A J 2020 Swimmers' wake structures are not reliable indicators of swimming performance *Bioinspir. Biomim.* **15** 024001

[21] Floryan D, Van Buren T and Smits A J 2018 Efficient cruising for swimming and flying animals is dictated by fluid drag *Proc. Natl Acad. Sci. USA* **115** 8116–8

[22] Lighthill M J 1960 Note on the swimming of slender fish *J. Fluid Mech.* **9** 305–17

[23] Lighthill J and Blake R 1990 Biofluiddynamics of balistiform and gymnotiform locomotion: I. Biological background, and analysis by elongated-body theory *J. Fluid Mech.* **212** 183–207

[24] Wu T Y-T 1961 Swimming of a waving plate *J. Fluid Mech.* **10** 321–44

[25] Neveln I D, Bale R, Bhalla A P S, Curet O M, Patankar N A and MacIver M A 2014 Undulating fins produce off-axis thrust and flow structures *J. Exp. Biol.* **217** 201–13

[26] Uddin M I and Curet O M 2018 Hydrodynamic and maneuvering control of an underwater vessel with undulating-fin propulsion *Bull. Am. Phys. Soc.* **63** Num. 13

[27] Bale R, Shirgaonkar A A, Neveln I D, Bhalla A P S, MacIver M A and Patankar N A 2014 Separability of drag and thrust in undulatory animals and machines *Sci. Rep.* **4** 7329

[28] Curet O M, Patankar N A, Lauder G V and MacIver M A 2011 Mechanical properties of a bio-inspired robotic knifefish with an undulatory propulsor *Bioinspir. Biomim.* **6** 026004

[29] Uddin M I and Curet O M 2018 Modeling and control of a bio-inspired underwater vessel with undulating-fin propulsion *OCEANS 2018 MTS/IEEE* (Charleston) pp 1–7

[30] Shirgaonkar A A, Curet O M, Patankar N A and MacIver M A 2008 The hydrodynamics of ribbon-fin propulsion during impulsive motion *J. Exp. Biol.* **211** 3490–503

[31] Liu H and Curet O M 2017 Propulsive performance of an under-actuated robotic ribbon fin *Bioinspir. biomim.* **12** 036015

[32] Liu H and Curet O M 2018 Swimming performance of a bio-inspired robotic vessel with undulating fin propulsion *Bioinspir. Biomim.* **13** 056006

[33] Sun X, Zhang J, Li H and Huang D 2018 Parametric study of an undulating plate in a power-extraction regime *J. Mech. Sci. Technol.* **33** 255–68

[34] English I, Liu H and Curet O M 2019 Robotic device shows lack of momentum enhancement for gymnotiform swimmers *Bioinspir. Biomim.* **14** 024001

[35] Lauder G and Tytell E 2006 Hydrodynamics of undulatory propulsion *Fish Biomechanics* (San Diego, CA: Elsevier) pp 425–68

[36] Wu T Y 2011 Fish swimming and bird/insect flight *Annu. Rev. Fluid Mech.* **43** 25–58

[37] Ruiz-Torres R, Curet O M, Lauder G V and MacIver M A 2013 Kinematics of the ribbon fin in hovering and swimming of the electric ghost knifefish *J. Exp. Biol.* **216** 823–34